

Unusual ferroelectric and magnetic phases in multiferroic 2H-BaMnO₃ ceramics

Stanislav Kamba,^{1,*} Dmitry Nuzhnyy,¹ Maxim Savinov,¹ Pierre Tolédano,² Valentin Laguta,¹ Petr Brázda,¹ Lukáš Palatinus,¹ Filip Kadlec,¹ Fedir Borodavka,¹ Christelle Kadlec,¹ Petr Bednyakov,¹ Viktor Bovtun,¹ Martin Kempa,¹ Dominik Kriegner,³ Jan Drahokoupil,¹ Jan Kroupa,¹ Jan Prokleška,³ Kamal Chapagain,⁴ Bogdan Dabrowski,⁴ and Veronica Goian¹

¹*Institute of Physics, Czech Academy of Sciences,
Na Slovance 2, 182 21 Prague 8, Czech Republic*

²*Laboratoire de Physique de Systèmes complexes, Université de Picardie, 80000 Amiens, France*

³*Faculty of Mathematics and Physics, Charles University,
Ke Karlovu 5, 121 16 Prague 2, Czech Republic*

⁴*Department of Physics, Northern Illinois University, DeKalb, IL, USA*

(Dated: October 3, 2018)

The structural phase transition in hexagonal BaMnO₃ occurring at $T_C=130$ K was studied in ceramic samples using electron and X-ray diffraction, second harmonic generation as well as by dielectric and lattice dynamic spectroscopies. The low-temperature phase (space group $P6_3cm$) is ferroelectric with a triplicated unit cell. The phase transition is driven by an optical soft mode from the Brillouin-zone boundary [$q = (\frac{1}{3}, \frac{1}{3}, 0)$]; this mode activates in infrared and Raman spectra below T_C and it hardens according to the Cochran law. Upon cooling below T_C , the permittivity exhibits an unusual linear increase with temperature; below 60 K, in turn, a frequency-dependent decrease is observed, which can be explained by slowing-down of ferroelectric domain wall motions. Based on our data we could not distinguish whether the high-temperature phase is paraelectric or polar (space groups $P6_3/mmc$ or $P6_3mc$, respectively). Both variants of the phase transition to the ferroelectric phase are discussed based on the Landau theory. Electron paramagnetic resonance and magnetic susceptibility measurements reveal an onset of one-dimensional antiferromagnetic ordering below ≈ 220 K which develops fully near 140 K and, below $T_N \approx 59$ K, it transforms into a three-dimensional antiferromagnetic order.

I. INTRODUCTION

In proper ferroelectrics, the polarization plays the role of the order parameter (OP) and at the Curie temperature T_C , a large peak in the temperature dependence of the permittivity $\varepsilon'(T)$ is observed due to softening of some polar excitation.^{1,2} In displacive proper ferroelectrics, this excitation corresponds to a polar phonon active in far-infrared (IR) spectra in both paraelectric and ferroelectric (FE) phases. At T_C , $\varepsilon'(T)$ exhibits a maximum due to the phonon softening, since the soft-phonon frequency ω_{SM} follows the Cochran law, $\omega_{SM}(T) = A\sqrt{T - T_C}$, and according to the Lyddane-Sachs-Teller relation, the static permittivity $\varepsilon'(T) \propto 1/\omega_{SM}^2(T)$.^{1,2} In proper ferroelectrics with order-disorder-type phase transitions, phonons are stable; by contrast, these compounds exhibit a dielectric relaxation whose frequency ω_r is located in the MHz–GHz region.³ On cooling towards T_C , this frequency decreases according to a modified Cochran law, $\omega_r = A'(T - T_C)$, which induces an anomaly in $\varepsilon'(T)$ at T_C . As the value of ε' near T_C is strongly frequency-dependent, a maximum or minimum in $\varepsilon'(T)$ at T_C is observed if the measuring frequency is lower or higher than ω_r , respectively.³ It is worth noting that many proper ferroelectrics exhibit phase transitions corresponding to a crossover from displacive to order-disorder type^{4–7}. In such a case, some polar phonon softens on cooling far above T_C , but this softening ceases at some temperature closer to T_C as an additional soft dielectric relaxation (called a central mode) appears.^{1,4,5}

In pseudoproper and improper ferroelectrics, the OP is represented by another quantity such as strain, the antiferromagnetic (AFM) OP, the eigenvector of a phonon with a wavevector off the Brillouin zone (BZ) center,^{8–10} charge or orbital ordering.¹¹ In these cases the FE polarization below T_C arises due to coupling of the polarization with the primary OP and usually only a small dielectric anomaly appears near T_C . Proper and pseudoproper ferroelectrics exhibit equitranslational phase transitions, whereas improper FE phase transitions are non-equitranslational, i.e., below T_C , a multiplication of the unit cell occurs. The pseudoproper ferroelectrics include most of the spin-induced ferroelectrics (type-II multiferroics) featuring an effective bilinear coupling of the polarization with the AFM OP.¹⁰ Applications of anharmonic lattice interactions in improper ferroelectrics for the design of multiferroics are summarized in a recent review.¹¹

Type-I multiferroics are mostly proper ferroelectrics—their polarization exists independently of their magnetization. The exceptions include hexagonal RMnO₃ materials (R = Sc, Y, Dy–Lu) which exhibit improper FE phase transitions at 900–1300 K¹² connected with a tripling of the unit cell below T_C , and AFM phase transitions around 70–130 K.^{13,14} Their structural phase transitions were theoretically predicted to be induced by a K_3 -symmetry soft mode from the BZ boundary [$q = (\frac{1}{3}, \frac{1}{3}, 0)$]¹⁵; however, this was never confirmed, because the required inelastic neutron or X-ray scattering experiments above $T_C \approx 1000$ K are quite difficult to perform. Moreover, the phonons at high temperatures are

always heavily damped, which makes their detection even more difficult. The soft mode should become IR and Raman active below T_C , but no such mode was revealed in recent IR¹⁶ or Raman studies.¹⁷

The lattice dynamics were studied also in other improper ferroelectrics, such as $\text{Gd}_2(\text{MoO}_4)_3$ ¹⁸ or boracites^{19,20}, but no soft mode was detected^{19,20} or it was markedly overdamped and therefore it was seen as a central mode.¹⁸ Recently, Varignon and Ghosez²¹ predicted an improper FE phase transition in the two-layered hexagonal BaMnO_3 (further denoted as 2H- BaMnO_3). Interestingly, in analogy with RMnO_3 , the phase transition should be driven by a K_3 -symmetry soft mode with $q = (\frac{1}{3}, \frac{1}{3}, 0)$ and the polarization should be induced by a coupling between the soft mode and a hard zone-center mode of Γ_2^- symmetry.

Although most ABO_3 compounds crystallize in the perovskite structure, this does not hold true for BaMnO_3 whose perovskite polymorph is unstable; instead, it crystallizes in a more stable hexagonal form with layers of face-sharing MnO_6 octahedra. The arrangement of these layers is determined by the synthesis conditions (temperature and atmosphere) which may produce oxygen vacancies. As their concentration increases, the double-layered structure (i.e., $Z = 2$) gradually transforms to 15, 8, 6, 10 and 4-layered ones.^{22,23} In this paper we deal with the stoichiometric 2H- BaMnO_3 , whose room-temperature crystal structure has raised a long-standing discussion. Some authors reported a non-polar space group $P6_3/mmc$ ($Z = 2$)^{21,24,25} but other structural and vibrational studies proposed a polar one, $P6_3mc$ ($Z = 2$).^{26,27} Also the low-temperature crystal structure was uncertain for a long time. Cussen and Battle, who had refined the crystal structure at 80 K, concluded that the space group is $P6_3cm$ and $Z = 6$. Only very recently Stanislavchuk *et al.* confirmed this structure by neutron diffraction, finding the structural phase transition at $T_C = 130 \pm 5$ K.²⁷ They investigated also the lattice dynamics of 2H- BaMnO_3 using Raman scattering and far-IR ellipsometry, detecting much fewer modes than the number predicted by the factor-group analysis, and no soft mode. At low temperatures, 2H- BaMnO_3 exhibits an AFM order, but the details are also controversial; according to Christensen and Ollivier,²⁴ below the Néel temperature of $T_N = 2.4$ K, the spins would be directed along the c axis, while a newer work by Cussen and Battle²⁵ reported $T_N = 59$ K and the spin directions were identified in (001) planes.

Below we present results of a set of experiments on 2H- BaMnO_3 using X-ray and electron diffraction, second harmonic generation (SHG), magnetic and EPR studies, dielectric, microwave, THz time-domain, Raman and IR spectroscopies. In the diffraction experiments, we confirmed the non-equitranslational phase transition to occur at $T_C = 130$ K. Furthermore, below T_C , we observed an IR- and Raman-active soft phonon from the BZ boundary which drives the phase transition. We show that dielectric permittivity and FE polarization exhibit

an unusual temperature behavior, which we discuss based on the Landau theory. Above $T_N \approx 59$ K, magnetic susceptibility and EPR intensity do not follow the Curie-Weiss behavior, which is related to a one-dimensional AFM order or short-range magnetic correlations existing within at least 160 K above T_N .

II. EXPERIMENTAL DETAILS

2H- BaMnO_3 was synthesized following the conventional ceramic fabrication method from high-purity (99.999 %) BaCO_3 and MnO_2 . The starting mixture was wet-ball-milled for 12 hours in alcohol using an agate container. After drying, the resulting slush was calcined in oxygen at 800 °C. The black powder was subsequently re-ground in an agate mortar and pressed into high-density pellets. Several additional firings in oxygen with intermediate grindings were carried out at increasing temperatures in the range of 950–1150 °C, followed by natural cooling to room temperature for ca. 12 hours. To examine the phase purity of our samples, after each firing, powder X-ray diffraction (XRD) measurements were carried out using a Rigaku D/MAX powder diffractometer with CuK_α radiation in the $2\theta = 20$ – 70° range. In agreement with Ref. 22, the single-phase 2H- BaMnO_3 formed only below 1125 °C whereas above this temperature, the 15-layered impurity phase was observed. The final ceramic samples were thus prepared by firing in oxygen at 1100 °C for 24 hours. Their structure was then again verified by XRD—see the diffraction pattern in Fig. 1, whereby a single-phase 2H- BaMnO_3 composition was confirmed.

Low-temperature XRD was performed using a custom-adapted Siemens D500 diffractometer equipped with a closed-cycle Sumitomo Heavy Industries cryocooler enabling cooling down to 3 K. We used the $\text{Cu-K}\alpha_{1,2}$ radiation and the Bragg-Brentano geometry with source-sample and sample-detector distances of 330 mm. The measurement was performed with a fixed divergence slit size, resulting in a primary-beam divergence of 0.44° . A MYTHEN 1K linear detector and an optimized integration procedure,²⁸ avoiding geometrical defocussing, were used to obtain the powder diffraction patterns. The lattice parameters were determined by Pawley mode in the Rietveld analysis²⁹ using the Topas software tool.³⁰

Electron diffraction measurements were performed on a Philips CM120 transmission electron microscope equipped with a Digistar Nanomegas precession device and a Olympus Veleta CCD camera. The data were collected in the precession electron-diffraction tomography regime³¹ with a precession angle of 0.6° and a tilt step of 0.6° . A part of the pellet was crushed in an agate mortar and dispersed on a holey-carbon-coated Cu grid. The sample was inserted in a cooling holder with the low-temperature limit of 97 K. The data were processed with the PETS software³² and the structures refined with the Jana2006 software³³ using the dynamical refinement method^{34,35}. Selected crystals with lateral dimensions of

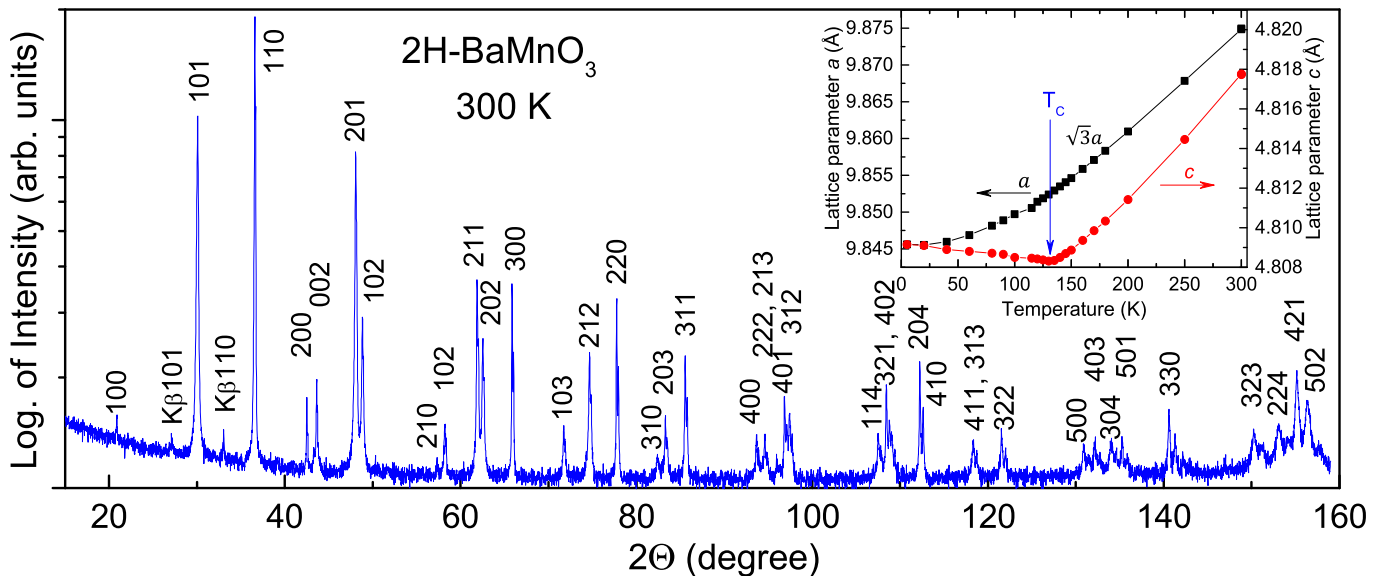


FIG. 1: Room-temperature XRD pattern measured in the Bragg-Brentano geometry with a Co anode and the K_{α} line. A β filter was used to avoid the K_{β} radiation. Nevertheless, some minor diffraction peaks for the K_{β} radiation were observed. All diffraction spots were assigned, and no extra peaks from other phases were detected. Inset shows the temperature dependences of lattice parameters obtained by XRD, which turn out to be the same as those obtained previously for single crystals of 2H-BaMnO₃ in Ref. 27 using neutron diffraction.

less than 500 nm (see Fig. 1 in the Supplemental Material [36]) were cooled down to 99 K. A full 3D electron diffraction data set (completeness 94%) was collected at temperatures from 99 to 240 K. Finally, the crystal was cooled again to 120 K to check for data consistency and possible radiation damage.

Radio-frequency dielectric measurements were performed using a NOVOCONTROL Alpha-AN impedance analyzer in conjunction with a JANIS ST-100 cryostat (5–300 K). Gold electrodes were evaporated on sample plates with a diameter of 3 mm and thicknesses of 250 and 129 μm . Dielectric hysteresis loops were measured at a frequency of 50 Hz with a testing voltage of 1 V, using a custom-made Sawyer-Tower bridge. Pyrocurrent measurements (at a heating rate of 5 K/min after a cooling with a bias of 40 kV/cm) used a KEITHLEY 6517A Electrometer high resistance meter; the resulting polarization was calculated by subtracting the thermally stimulated current related to charged defects.

For microwave dielectric measurements, the method of a composite dielectric resonator^{37,38} was used. $\text{TE}_{01\delta}$ resonance modes were excited first in the base cylindrical dielectric resonator and then in the composite dielectric resonator, consisting of the base and the sample in the shielding cavity. The disk-shaped sample had the same diameter (~ 13 mm) as the base and a thickness of 1.9 mm. A comparison of the resonance frequencies and quality factors of the base and composite resonators allowed for calculating the dielectric parameters of the sample at the resonance frequency (~ 6 GHz). Temperature dependencies of the resonance frequencies and quality factors were measured using an AGILENT E8364B

vector network analyzer and a Janis closed-cycle He cryostat (10 K–400 K).

SHG measurements were performed in order to confirm a possible polar structure above T_C . A Q-switched Nd-YAG laser (7 ns pulses with a variable energy, $\lambda = 1064$ nm, 20 Hz) was used as a light source and, after a reflection on the sample, the filtered second harmonic signal at 532 nm was detected by a photomultiplier and boxcar integrator.

Low-temperature IR reflectivity measurements in the frequency range 30–670 cm^{-1} (or, equivalently, 1–20 THz) were performed using a Bruker IFS-113v Fourier-transform IR spectrometer equipped with a liquid-He-cooled Si bolometer (1.6 K) serving as a detector. Room-temperature mid-IR spectra up to 5000 cm^{-1} were obtained using a pyroelectric deuterated triglycine sulfate detector. THz complex transmission from 3 to 100 cm^{-1} was measured using a custom-made time-domain spectrometer utilizing a Ti:sapphire femtosecond laser. For the low-temperature IR reflectivity and THz complex transmission spectroscopy, Oxford Instruments Optistat continuous-He-flow cryostats with polyethylene and mylar windows, respectively, were used. THz spectra with magnetic field were measured in an Oxford Instruments Spectromag cryostat with a superconducting magnet, capable of applying an external magnetic field of up to 7 T. The spectra were recorded in the Voigt geometry with both polarizations, i.e., the electric vector of the THz radiation parallel or perpendicular to the external magnetic field.

For Raman studies, a Renishaw RM1000 Micro-Raman spectrometer equipped with a CCD detector and

Bragg filters was used. The experiments were performed in the backscattering geometry within the $10\text{--}800\text{ cm}^{-1}$ range using an Ar^+ ion laser with the wavelength of 514.5 nm and an Oxford Instruments Optistat optical continuous-He-flow cryostat. Further, using a Quantum Design MPMS XL 7T and PPMS 9T instruments, we carried out measurements of the magnetic susceptibility, magnetization and heat capacity in the temperature interval of $2\text{--}400\text{ K}$.

Magnetic resonance measurements were performed using a conventional electron paramagnetic resonance (EPR) spectrometer operating at $9.2\text{--}9.8\text{ GHz}$ and within $T = 10\text{--}570\text{ K}$. An Oxford Instrument cryostat was used for temperature measurements in the range from 10 to 300 K . The measurements at $T > 300\text{ K}$ utilized a nitrogen-gas variable temperature control system.

III. RESULTS AND DISCUSSION

A. Structural properties

The Rietveld analysis of our XRD data taken at various temperatures down to 5 K (see Figs. 2–4 in the Supplemental Material [36]) confirmed the structural phase transition at $T_C = 130\text{ K}$. It manifests itself mainly by a negative thermal expansion coefficient of the c lattice parameter below T_C (see inset in Fig. 1), which was observed recently also by Stanislavchuk *et al.*²⁷ using neutron diffraction. We would like to emphasize that a similar negative thermal expansion of the lattice was observed below improper FE phase transitions in YMnO_3 and HoMnO_3 , respectively,^{39,40} which have the same space groups as 2H-BaMnO_3 .

In our XRD patterns, below T_C , no satellites expected for a tripled unit cell were detected, due to their extreme weakness. Nevertheless, based on our results of electron diffraction, we refined the low-temperature structure in the $P6_3cm$ space group with the unit cell tripling in the hexagonal plane. In the high-temperature phase, the structure refinement was possible in polar $P6_3mc$ and non-polar $P6_3/mmc$ space groups ($Z = 2$) with almost the same R factors within the error margin (see Figs. 4 in the Supplemental Material [36]). Therefore, based on the XRD measurements alone, we cannot decide whether the structure is polar or not.

Electron diffraction was measured down to 99 K . At each temperature the crystal structure was refined using the full-matrix least-square refinement and using the dynamical diffraction theory to calculate model intensities. The diffraction patterns from 140 to 240 K correspond to 2H-BaMnO_3 without any presence of other polytypes (see Fig. 2). Below T_C , the crystal undergoes a reversible phase transformation to the $P6_3cm$ space group with a tripled unit cell (see the satellite reflections in Figs. 2 and 3), in agreement with Ref. 27. No other remarkable features were detected in the diffraction patterns. The intensities of the superlattice reflections in the

$hk0$ plane (not shown) are negligible, implying that the polarization-inducing atomic shifts of Ba cations against the MnO_6 octahedra at the phase transition occur predominantly along the c axis.

The spontaneous polarization of the low-temperature phase is related to the shifts of the cations out of the high-symmetry positions. Assuming that Mn atoms occupy exactly the centers of the MnO_6 octahedra, the polarization is proportional to the mean difference of the shifts of Ba and Mn atoms from their high-symmetry positions. This offset equals 0.0079 c at 99 K , 0.0080 c at 116 K , and 0.0093 c at 130 K . At the same time, the relative shift of the $\text{Mn}(1)\text{O}_3$ and $\text{Mn}(2)\text{O}_3$ chains along c decreases from 0.0284 c at 99 K to 0.0214 c at 116 K and 0.0157 c at 130 K . Thus, whereas the shift of Mn atoms decreases towards the phase transition, the estimated polarization remains approximately constant and does not vanish at T_C . This indicates that the high-temperature phase could be also polar.

On heating, the intensities of the superlattice reflections gradually decrease (see Fig. 3) and they level off above 170 K . Simultaneously, additional diffuse scattering appears above T_C , testifying to short-range (dynamic) nanoregions with a polar $P6_3cm$ symmetry and a tripled unit cell, persisting at least up to 170 K . The diffuse scattering can be explained by a mutual shift of the nearest columns of MnO_6 octahedra whereas the next-nearest ones are shifted reversely. Above T_C , if the weak superlattice reflections are neglected, the structure can be refined again in both $P6_3/mmc$ and $P6_3mc$ space groups with almost the same figures of merit and almost identical structure models. In absence of inversion twins, this would indicate that the structure is centrosymmetric, as there is no evidence for symmetry lowering. However, we cannot exclude the presence of nanodomains twinned by inversion, so we cannot distinguish whether the high-temperature phase is polar or unpolar.

SHG is a powerful method for determining polar order, because it senses the second-order susceptibility which is non-zero only in non-centrosymmetric crystal structures. The results were, however, not quite conclusive. Due to a high absorption and a low damage threshold we could employ only rather weak pulses, which reduced the detection sensitivity. At room temperature, we were able to detect a signal somewhat stronger than the noise level. However, any surface of the sample is non-centrosymmetric, so it can also contribute to the detected SHG signal. In this case it was difficult to separate both possible contributions. On cooling, the signal remained almost constant, only around $T_C \approx 130\text{ K}$ a small increase was observed; this was, unfortunately, not quite reproducible. Altogether, the quality of the SHG data was insufficient to determine reliably whether the high-temperature phase is non-centrosymmetric. For that reason, below we discuss our results considering both options, i.e., that the phase above T_C may be polar or non-polar.

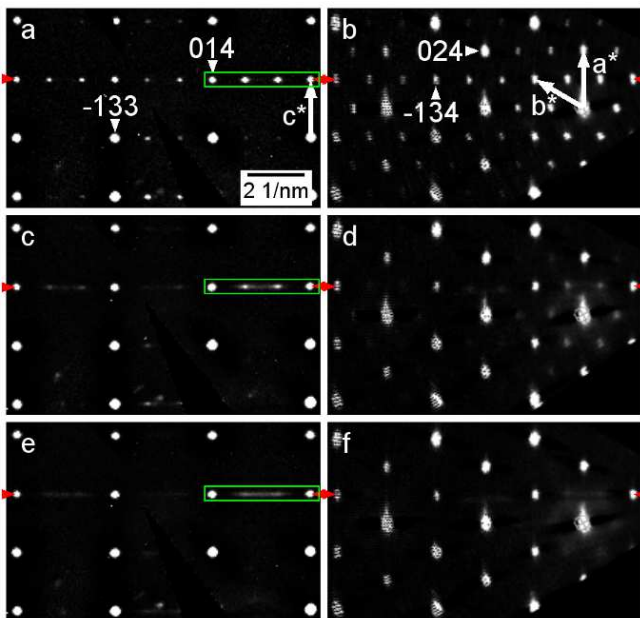


FIG. 2: Reciprocal space cuts through (a) $(h + \frac{1}{2})(-2h)l$ and (b) $hk4$ planes measured by electron diffraction tomography at 99 K. The cut planes are perpendicular to each other, intersecting at the line marked by red arrows. Parts (c)–(f): same cuts obtained at 130 K and 170 K. The green boxes indicate the area used to calculate the intensity profiles in Fig. 3.

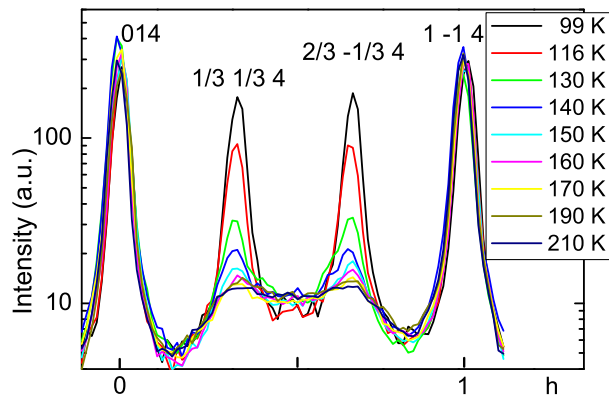


FIG. 3: Electron diffraction intensity profiles of the four reflections along the $hk4$ line ($k = 1 - 2h$) at different temperatures. The inner two peaks reveal the superstructure.

B. Dielectric properties

Assuming that both phases are polar (space groups $P6_3mc$ and $P6_3cm$ for the high- and the low-temperature one, respectively), one may ask whether these phases are FE, i.e., if they have a switchable polarization. To investigate this issue, we have performed detailed dielectric and lattice-dynamics studies.

The temperature dependence of the permittivity $\epsilon'(T)$ shows a rather unusual behavior: upon cooling, ϵ' between 0.9 MHz and 6 GHz is temperature independent

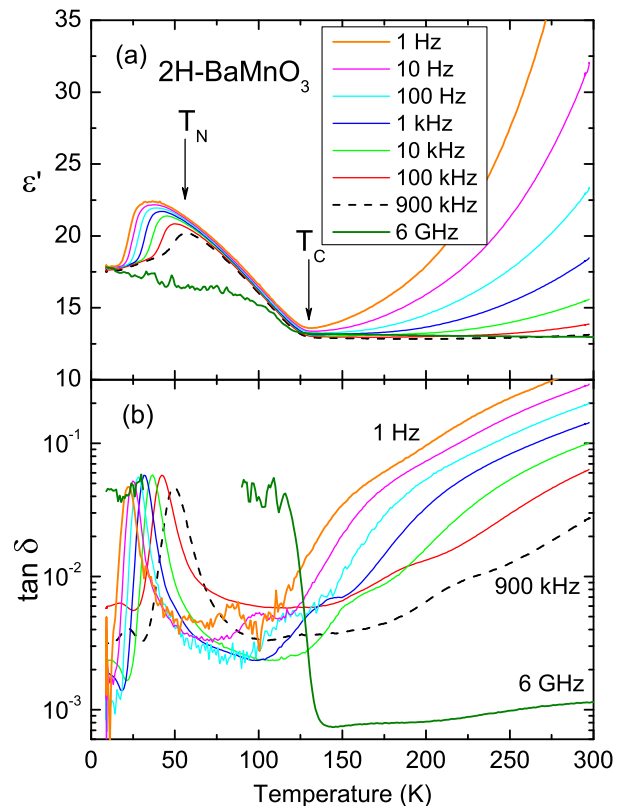


FIG. 4: Temperature dependence of (a) dielectric permittivity and (b) dielectric loss of 2H-BaMnO₃ ceramics measured at various frequencies. The values of $\tan \delta$ at 6 GHz in the temperature interval between 30 and 90 K are missing due to high losses.

down to T_C , and below it increases—see Fig. 4. The absence of a peak at T_C and the gradual increase in ϵ' below T_C are typical of nonferroic second order phase transitions (see Fig. 1 in Ref. 41) which supports the conjecture of a transition between two polar phases $P6_3mc$ ($Z = 2$) and $P6_3cm$ ($Z = 6$). A hypothetical phase transition from a nonpolar $P6_3/mmc$ ($Z = 2$) to a $P6_3cm$ ($Z = 6$) phase should be improper FE²¹ and, in this case, a jump or a small peak in ϵ' would be expected at T_C .^{8,9} Below ≈ 60 K, ϵ' decreases, but this decrease is strongly frequency dependent, reminding of a relaxor FE behavior. This dielectric dispersion is apparently caused by slowing down of domain-wall vibrations, as the relaxation times τ obtained from the maxima of dielectric losses $\epsilon''(f, T)$ [see Fig. 4(b)] follow the Arrhenius law $\tau = \tau_0 \exp \frac{E_a}{k_B T}$ with the following parameters: $E_a = 0.04803$ eV (557.4 K) and $\tau_0 = 3.15 \times 10^{-12}$ s (see Fig. 5 in the Supplemental Material [36]). A qualitatively similar effect was observed also in other ferroelectrics.⁴² The contribution of domain-wall vibration to ϵ' was strongly reduced when it was measured in a bias electric field of 11.3 kV/cm (see Fig. 6 in the Supplemental Material [36]).

The dielectric dispersion observed above T_C at low fre-

quencies is caused by the Maxwell-Wagner polarization, due to different values of conductivity of grains and grain boundaries in the ceramics.⁴³

Polarization hysteresis-loop measurements were performed in a sinusoidal AC field. At higher temperatures, they revealed lossy elliptical loops due to conductivity, down to 170 K when the loops become a straight line typical of paraelectrics. Below 170 K the loops open again, but although they have sharp ends, they do not saturate. Below T_C , the loops have a slim S-shape [see Fig. 5(a)] typical of relaxors or weak ferroelectrics. The remnant polarization $P_r \equiv P(E = 0)$ exhibits an unusual temperature behavior [see Fig. 5(b)]. At higher temperatures, it shows high values due to extrinsic conductivity. Upon cooling, P_r drops and it becomes zero at 170 K when the paraelectric loop is seen. On further cooling, P_r increases, saturates near T_C and increases again. Below ≈ 60 K it starts to decrease and, finally, it becomes pinched (i.e., $P_r^+ = P_r^-$; here P_r^+ and P_r^- mark the remnant polarization for electric field going to zero from positive and negative sites, respectively) at $T^* = 26$ K in zero electric field and opens only for $E \neq 0$, which reminds of antiferroelectrics. On subsequent cooling the hysteresis loop opens again.

What is the origin of this effect? Constrained hysteresis loops were reported already in many doped ferroelectrics like hard $\text{Pb}(\text{Zr},\text{Ti})\text{O}_3$ ^{44,45} and they were explained by an internal bias field $E_i(t)$ due to defects. According to Ref. 44, this field increases with doping, but the hysteresis-loop distortion disappears after a repeated cycling. This so called ‘‘hysteresis relaxation’’ obeys a time law in the form $E_i(t) \propto \exp(-t/\tau)$ and it is found to be a both field- and thermally activated process.⁴⁴ However, the behavior observed in 2H-BaMnO₃ is different: the pinched hysteresis loops at 26 K remain unchanged after many cycles (measured at 50 Hz for 10 min.). Moreover, they open again at lower temperatures, which would be excluded by the above-mentioned mechanism which assumes a thermally stimulated process.

Levanyuk and Sannikov investigated theoretically improper ferroelectrics using the phenomenological Landau theory⁸ and, based on the temperature dependencies of the coefficients in the Landau expansion, they predicted that the hysteresis loops may get pinched and take up shapes similar to antiferroelectric ones. Nevertheless, they did not predict a reentrant phase transition to a FE state with a single open hysteresis loop. Moreover, for 26 K, Fig. 5 shows a double hysteresis loop which is not one typical of antiferroelectrics with some critical electric fields E_{c1} and E_{c2} ; our loop is open at any $E \neq 0$. Interestingly, the loop is pinched at $E = 0$, but we observed that $P_r^+ = P_r^- \neq 0$ (Fig 5b). We are not aware of any published report of this effect, which can be explained probably by the fact that few improper ferroelectrics were studied up to now and also by the low values of P_s in these materials, which make it difficult to measure the FE loops directly. Most probably, the pinching is caused by some defects, but we cannot ex-

clude some intrinsic origin.

At all temperatures, the loops are very slim and the polarization is very small, which can rise doubts about the ferroelectricity in 2H-BaMnO₃. For that reason we have measured the pyroelectric current [zero-field heating after a cooling at 40 kV/cm, (see Fig. 7(a) in the Supplemental Material [36])] from which we calculated the spontaneous polarization $P_s(T)$ [see Fig. 5(c)]. One can see the onset of P_s below 175 K, its increase at T_C and saturation below 100 K. The non-zero values of P_s and P_r above T_C can be explained by the persistence of clusters of the low-temperature phase above T_C , which is confirmed also by the electron diffraction.

Nevertheless, we should note that the $P_s(T)$ was calculated from the pyrocurrent by subtracting both high- and low-temperature increase (see Fig. 7 in the Supplemental Material [36]), which we attribute to thermally stimulated current of migrating defects (mainly oxygen vacancies and related Mn^{3+}). If we subtract only high-temperature contribution, the calculated polarization would be unrealistically one order of magnitude higher. In such a case, P_s would linearly increase on cooling below 180 K (as much as 50 K above T_C , see Fig. 7(b) in the Supplemental Material [36]), exhibiting no anomaly near T_C . Such a linear dependence of $P_s(T)$ can be expected below an improper FE phase transition,^{8,9} but in that case the unit cell should triple already at 180 K. One can argue that T_C could be shifted by the external electric field of 40 kV/cm used before the pyrocurrent measurements. However, we also investigated $\epsilon'(T)$ with an external electric field of 11.3 kV/cm and we observed no shift in T_C . For that reason we believe that the current detected below 100 K is a thermally stimulated one which, for a proper polarization calculation, should be subtracted, and that the phase transition at $T_C = 130$ K is nonferroic between two polar phases.

C. Phonon spectra

Based on the diffraction experiments alone, we cannot unambiguously distinguish between nonpolar $P6_3/mmc$ and polar $P6_3mc$ space groups in the high-temperature phase. Lattice-vibrations spectra can yield useful information, because the phonon selection rules are different in different space groups. We have performed a factor-group analysis of phonons, where we used site symmetries of all atoms known from structural refinements²⁵ and group tables in Ref. 46. If, above T_C , 2H-BaMnO₃ crystallizes in the $P6_3/mmc$ (D_{6h}^4) structure with $Z = 2$, the zone-center phonons have the following symmetries:

$$\begin{aligned} \Gamma_{D_{6h}^4} = & 3A_{2u}(z) + 4E_{1u}(x, y) + 2E_{2u} + 2B_{2u} + \\ & + A_{1g}(x^2 + y^2, z^2) + A_{2g} + 2B_{1g} + B_{1u} + \\ & + E_{1g}(xz, yz) + 3E_{2g}(x^2 - y^2, xy). \end{aligned} \quad (1)$$

Here x , y , and z in parentheses mark the electric polarizations of the IR radiation for which the phonons are

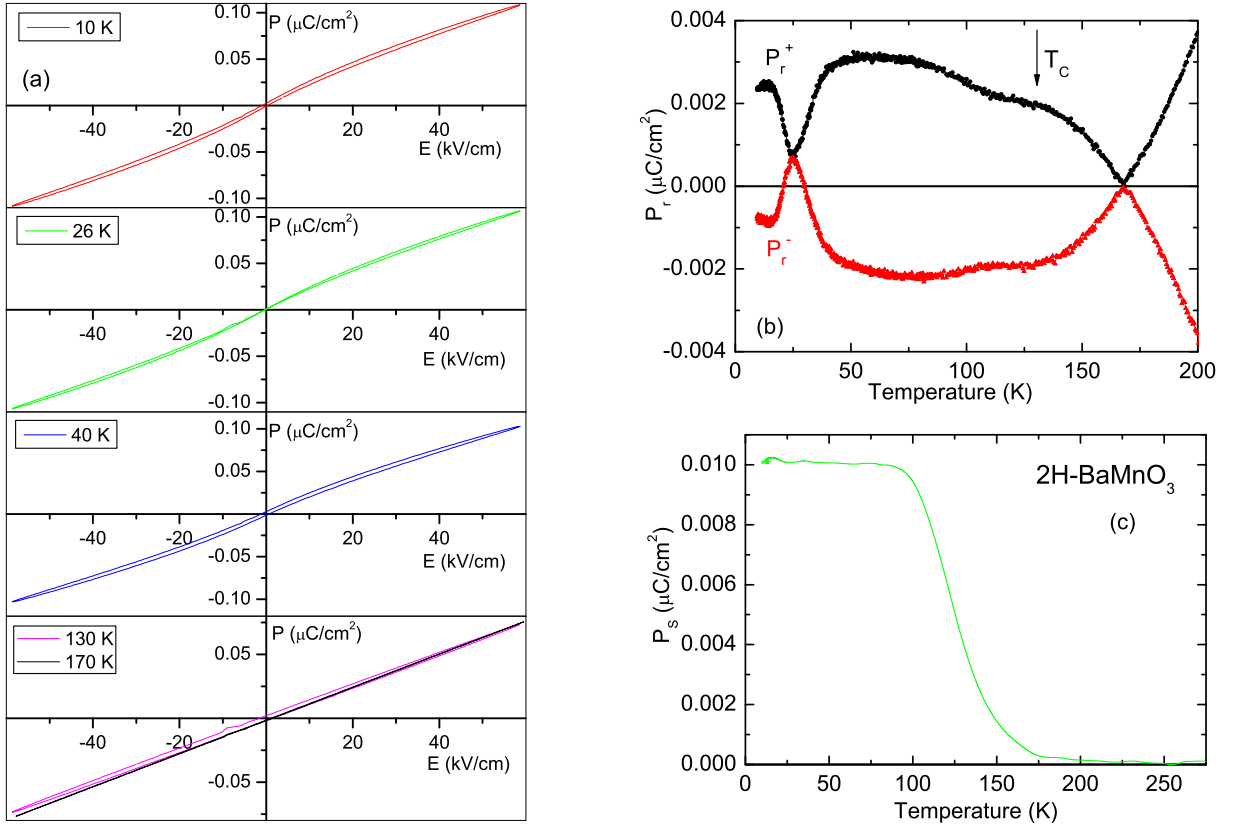


FIG. 5: (a) FE hysteresis loops taken at selected temperatures. Note the different scale for P at $T = 130$ K and 170 K; The latter one is paraelectric, i.e., not opened. Temperature dependence of (b) remnant $P_r(T)$ and (c) spontaneous $P_s(T)$ polarization calculated from pyrocurrent after subtraction of the assumed thermo-stimulated current due to defect migration. Here we would like stress, the polarization is non-zero in the high-temperature phase, here plotted $P_s(T)$ is just enhanced polarization due to phase transition to low-temperature phase.

IR active, whereas the rest of the symbols in parentheses are components of the Raman tensor. Phonons without parentheses are silent. Except for two acoustic phonons ($A_{2u} + E_1$), five IR-active and another five Raman-active phonons can be expected in the spectra.

If the high-temperature phase has a polar $P6_3mc$ (C_{6v}^4) structure with $Z = 2$, the phonons from the Γ point of the BZ have the following symmetries :

$$\Gamma_{C_{6v}^4} = 4A_1(z, x^2 + y^2, z^2) + 5E_1(x, y, xz, yz) + A_2 + B_1 + 4B_2 + 5E_2(x^2 - y^2, xy) \quad (2)$$

After subtracting two acoustic phonons, 7 IR- and Raman-active and five only Raman-active phonons are predicted in the spectra.

A phase transition connected with a tripling of the unit cell (and folding of the BZ) should exhibit a noticeable change of the selection rules for activation of phonons in IR and Raman spectra. The factor-group analysis of phonons in the low-temperature $P6_3cm$ (C_{6v}^3) structure with $Z = 6$ yields:

$$\Gamma_{C_{6v}^3} = 9A_1(z, x^2 + y^2, z^2) + 15E_1(x, y, xz, yz) + 6A_2 + 9B_1 + 6B_2 + 15E_2(x^2 - y^2, xy). \quad (3)$$

In this case, after subtracting two acoustic phonons, 22 modes ($8A_1 + 14E_1$) should be IR- and Raman-active and additional 15 E_2 -symmetry modes Raman-active only.

To compare the predictions with experiments, we measured Raman scattering down to 5 K (see Fig. 8 in the Supplemental Material [36]) and obtained spectra similar to those reported by Stanislavchuk *et al.*²⁷ Namely, we observed 6 modes at 300 K and only 8 sharp modes at 5 K, i.e., one more than the number allowed in the $P6_3/mmc$ phase and much fewer than allowed in the FE phase (the mode frequencies are listed in Table 1). The only newly observed mode, activating below T_C near 15 cm^{-1} and hardening to 26 cm^{-1} on cooling, could not be seen in Ref. 27 where the Raman spectra were measured only above 100 cm^{-1} .

Fig. 6 shows the IR reflectivity spectra of 2H-BaMnO₃ ceramics which, surprisingly, exhibit no dramatic changes with temperature. Some modes sharpen slightly on cooling due to their decreasing damping, but the number of IR-active phonons does not increase below T_C , in contrast to expectations based on the selection rules discussed above. This must be related to the fact that the FE distortion is very small and the newly allowed modes in the FE phase are very weak and therefore not detectable

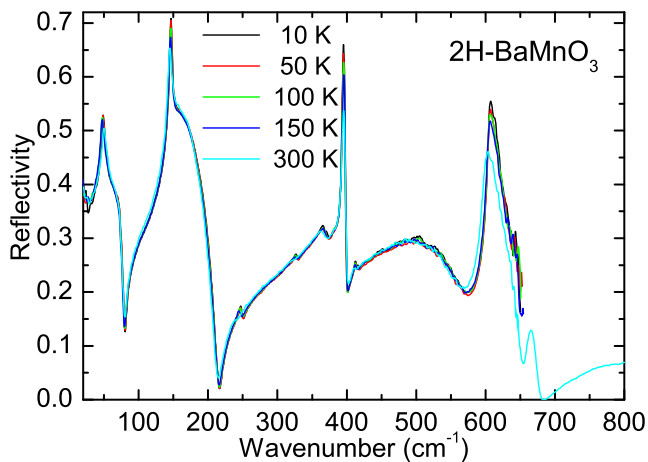


FIG. 6: IR reflectivity spectra of 2H-BaMnO₃ ceramics taken at various temperatures. The upper frequency limit of the low-temperature spectra is determined by the transparency of bolometer and cryostat windows.

in the IR and Raman spectra.

We measured the IR-active phonons also using the more sensitive time-domain THz transmission spectroscopy. As the sample was opaque between 50 and 80 cm⁻¹, where a strong reflection band is seen in Fig. 6, we present the THz spectra only below 35 cm⁻¹ (see Fig. 7); they reveal the same low-frequency mode as the Raman spectra. This weak mode appears at 100 K near 13 cm⁻¹ and it hardens on cooling, reaching the frequency of 26 cm⁻¹ at 5 K. Its temperature dependence (see inset of Fig. 7) follows the Cochran law, $\omega_{SM} = A\sqrt{T_C - T}$ with $T_C = 130$ K, implying that this is the soft mode driving the structural phase transition with unit cell tripling. Above T_C , this phonon has a wavevector $q = (\frac{1}{3}, \frac{1}{3}, 0)$ at the BZ boundary, so it cannot be observed in the IR or Raman spectra, which detect only phonons with $q = 0$. Below T_C the BZ folds, the phonon wavevector transforms to the BZ center and the soft mode activates in the THz and Raman spectra.

The complex dielectric spectra shown in Fig. 7 and the IR reflectivity spectra in Fig. 6 were fitted using a model consisting of a sum of damped Lorentzian oscillators.⁵ The dielectric strength $\Delta\epsilon_{SM}$ of the soft mode was found to be 0.2 at $T=5$ K and this value significantly decreased with increasing temperature. Thus, the contribution of the soft mode to the static permittivity is one order of magnitude lower than that of domain wall vibrations (5–10), but this fact is well known also from other ferroelectrics like PZT⁴⁷ and BaTiO₃⁴⁸.

It is possible to show that the soft mode cannot be due to an AFM resonance. In fact, we measured THz spectra with an external magnetic field of up to 7 T, which showed that the mode does not change with the field. This result questions a magnetic origin of the soft mode and supports its phonon origin. The absence of an AFM resonance in THz spectra is in agreement with the earlier

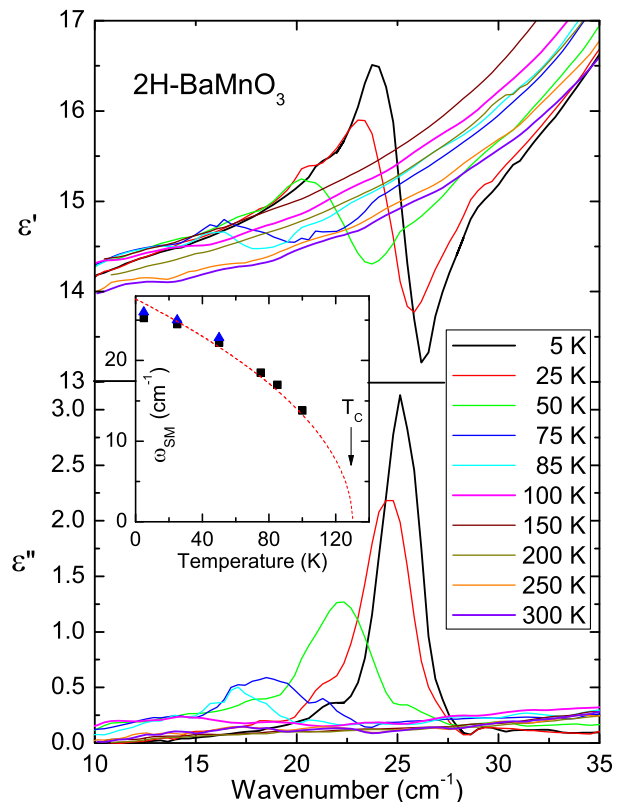


FIG. 7: THz complex dielectric spectra of 2H-BaMnO₃ ceramics, showing activation of a new phonon below $T_C = 130$ K. Inset shows the temperature dependence of the soft-mode frequency obtained from the THz (squares) and Raman (triangles) spectra. Dashed line is the result of the fit using Cochran law.

statement by Christensen *et al.*²⁴ about the same size of the structural and magnetic cells ($Z = 6$). The stability of the phonon parameters and of the THz permittivity with respect to external magnetic field also confirms a negligible magnetodielectric coupling in 2H-BaMnO₃.

We are coming back to the question whether the phase transition at T_C is an improper-FE one, from a non-polar $P6_3/mmc$ to a polar $P6_3cm$ structure, or a nonferroic one between two polar space groups $P6_3mc$ and $P6_3cm$. Since the diffraction experiments could not clearly distinguish between these two cases, older works^{21,24,25} claimed a non-polar symmetry at room temperature. Some newer papers^{26,27}, combining structural and lattice vibration studies, came to the conclusion that the high-temperature phase is polar, because two of the six observed phonons are both IR- and Raman-active.

In Table 1 we present mode frequencies observed in our IR and Raman spectra compared with those published previously²⁷. At room temperature, we can see only three out of seven modes allowed in the high-temperature polar phase, which are simultaneously IR and Raman active (at 410, 637 and 663 cm⁻¹). However, we detected altogether 16 IR-active modes, which significantly exceeds the number allowed in both possible high-temperature

TABLE I: Comparison of mode frequencies (in cm^{-1}) observed in our IR and Raman spectra at room temperature and 10 K and those published in Ref. 27, along with their symmetry assignments in polar space groups. Symmetry of heavily damped modes coming from crystal field or defects is not assigned. The modes in the high-temperature phase which cannot be accounted for by the factor-group analysis in Eq. (2), are marked by stars.

symmetry	note	300 K				10 K			
		ours	Ref. 27	ours	Ref. 27	ours	Ref. 27	ours	Ref. 27
		ω_{IR}	ω_{IR}	ω_{Raman}	ω_{Raman}	ω_{IR}	ω_{IR}	ω_{Raman}	ω_{Raman}
E_1		–	–	–	–	26	–	26	–
A_1		50	82	–	–	50	82	–	–
?	heavily damped	65	–	–	–	65	–	–	–
E_2		–	–	119.5	119	–	–	120.3	120
E_1		143	145	–	–	143	146.3	–	–
?	heavily damped	156*	–	–	–	156	–	–	–
?	sharp and weak	246*	–	–	–	246	–	–	–
?	heavily damped	294*	–	–	–	294	–	–	–
?	sharp and weak	327*	–	–	–	327	–	–	–
?	heavily damped	331*	–	–	–	331	–	–	–
E_2		–	–	–	344	–	–	–	344
A_1		362	–	–	–	362	–	369	368
?	heavily damped	378*	–	–	–	378	–	–	–
E_1		394	394.5	–	–	394	394	–	–
E_1		410	–	414.5	413	412	–	417	417
?	heavily damped	460*	–	–	–	460	–	–	–
A_1		–	–	490	487	–	–	490	492
?	heavily damped	499*	–	–	–	499	–	–	–
E_2		–	–	527	526	–	–	527	526
E_1		–	599	–	–	593	605	–	–
A_1		637	639	639	639	637	645	644	639
E_1		663	653	660	660	–	653	661	660

phases. Seven heavily damped modes (marked in Table 1) exhibit a constant damping on cooling, which is not a behavior typical of phonons. These broad bands can be crystal-field excitations of Mn^{4+} ,⁴⁹ or some defect-induced modes. The shape of the broad IR reflection bands reminds of spectra of crystalline glasses,⁵⁰ but our XRD did not reveal any traces of secondary amorphous phases in our ceramics. Although these heavily damped modes were not observed in IR-ellipsometric spectra of a 2H-BaMnO₃ single crystal²⁷, it is worth noting that these ellipsometric spectra were taken mostly in the hexagonal plane (i.e., sensitive to E_{1u} or E_1 symmetry spectra). Thus, the broad modes are probably active in the $\mathbf{E}||\mathbf{c}$ -polarized spectra. After subtracting these seven modes, nine of them remain, still more than allowed by the factor-group analyses in both possible high-temperature symmetries. The excess modes can be explained by the presence of dynamical nanoregions (as seen also in the electron diffraction above T_C) with a tripled unit cell; it is known that IR spectroscopy is extremely sensitive to a locally broken symmetry. Similar effects are well known also from relaxor ferroelectrics.⁵¹

In summary, it is not easy to identify clearly the space

group at $T > T_C$ as polar or nonpolar, based on IR and Raman spectra only. Also our structural, SHG and dielectric studies yielded no unambiguous result—the high-temperature phase can be either polar or nonpolar. In any case, the structural phase transition at T_C is non-equitranslational. We have discovered the soft mode which drives the phase transition; observations of this kind have been reported only rarely up to now. Previous lattice-dynamics studies of improper ferroelectrics revealed either no soft modes^{19,20} or merely an overdamped excitation resolved as a central mode¹⁸. Even in hexagonal RMnO₃ manganites (R = Sc, Y, Dy–Lu) which exhibit improper FE phase transitions^{12,15} analogous to 2H-BaMnO₃, no soft modes were reported.^{16,17}

Concerning non-ferroic phase transitions between two polar phases, very few materials with such phase transitions are known (examples include $\text{PbZr}_x\text{Ti}_{1-x}\text{O}_3$, $(\text{NH}_4)_2\text{H}_3\text{IO}_6$ or $\text{Na}_{1-x}\text{K}_x\text{NbO}_3$).⁴¹ They exhibit dielectric and phonon properties different from 2H-BaMnO₃—neither an underdamped soft mode nor an increase in ϵ' were observed below T_C . Only in one case, activation of new hard phonons due to unit-cell multiplication was reported.⁵² To our knowledge, no report of a soft mode

below a non-equitranslational nonferroic phase transition between two polar phases has been published yet.

D. Landau theory

The Landau theory of the improper FE phase transition in BaMnO₃ was published by Varignon *et al.*²¹ who explained the transition from a nonpolar $P6_3/mmc$ to polar $P6_3mc$ symmetry by a coupling of a K_3 -symmetry mode from the BZ boundary with a zone-center mode of Γ_2^- symmetry. In this case the free energy expansion in terms of their amplitudes Q_{K_3} and $Q_{\Gamma_2^-}$ has the form²¹

$$F(Q_{K_3}, Q_{\Gamma_2^-}) = \alpha_{20}Q_{K_3}^2 + \alpha_{02}Q_{\Gamma_2^-}^2 + \beta_{40}Q_{K_3}^4 + \beta_{04}Q_{\Gamma_2^-}^4 + \beta_{31}Q_{K_3}^3Q_{\Gamma_2^-} + \beta_{22}Q_{K_3}^2Q_{\Gamma_2^-}^2 \quad (4)$$

Here β_{31} and β_{22} express coefficients of the cubic and biquadratic coupling, respectively.

Let us assume that the non-equitranslational phase transition in 2H-BaMnO₃ is nonferroic between two polar space groups $P6_3mc$ and $P6_3cm$. In this case both phases exhibit a polarization along the z axis and the temperature dependence $P(T)$ in Fig. 5(c) corresponds only to the increase in polarization due to the structural phase transition.

For the wave vector $q = (\frac{1}{3}, \frac{1}{3}, 0)$, the observed symmetry change is induced by the two-dimensional irreducible representation K_1 of the $P6_3mc$ space group which is associated with the following complex matrices:

$$(C_1, C_3, C_3^2, m_x, m_y, m_{xy}) \rightarrow \begin{pmatrix} 1 & 0 \\ 0 & 1 \end{pmatrix}, \quad (5)$$

$$(C_2, C_6, C_6^5, m_1, m_2, m_3 | 0, 0, \frac{c}{2}) \rightarrow \begin{pmatrix} 0 & 1 \\ 1 & 0 \end{pmatrix}, \quad (6)$$

$$\vec{t}_1 = (a, 0, 0) \rightarrow \begin{pmatrix} \varepsilon^2 & 0 \\ 0 & \varepsilon \end{pmatrix}, \quad (7)$$

$$\vec{t}_2 = (0, a, 0) \rightarrow \begin{pmatrix} \varepsilon & 0 \\ 0 & \varepsilon^2 \end{pmatrix}, \quad (8)$$

$$\vec{t}_3 = (0, 0, c) \rightarrow \begin{pmatrix} 1 & 0 \\ 0 & 1 \end{pmatrix} \quad (9)$$

with $\varepsilon = \exp(2i\pi/3)$. Denoting the two-component order parameter associated with K_1 as $\eta_1 = \varrho \cos \theta$, $\eta_2 = \varrho \sin \theta$, the above matrices allow constructing the Landau free energy associated with the transition, which is

$$F = \frac{\alpha}{2}\varrho^2 + \frac{\beta_1}{3}\varrho^3 \cos 3\theta + \frac{\beta_2}{4}\varrho^4 + \frac{\gamma}{6}\varrho^6 \cos^2 3\theta. \quad (10)$$

Here a six-degree invariant has been included for a full description of all the phases of the phase diagram.

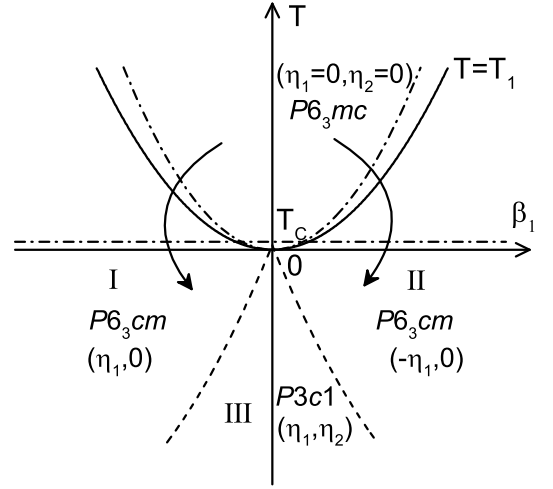


FIG. 8: Phase diagram corresponding to the free energy F given by Eq. 10 in the (T, β_1) plane. Dashed and solid curves represent the second and first-order transition limits, respectively. Dash-and-dot curves show the limits of stability. One of the two arrows indicates the thermodynamic path followed at the reported transition in 2H-BaMnO₃.

Minimizing F with respect to θ and ϱ one finds three possible low-symmetry stable phases, denoted I, II and III (see Fig. 8). Phases I and II, corresponding both to the equilibrium conditions ($\cos 3\theta = \pm 1, \varrho \neq 0$), have the same symmetry $P6_3cm$ with a tripling of the parent unit cell based on the basic translations $2\vec{t}_1 + \vec{t}_2, \vec{t}_2 - \vec{t}_1, \vec{t}_3$. However, they are anti-isostructural since one of them corresponds to $(\eta_1, \eta_2 = 0)$ and the other to $(-\eta_1, \eta_2 = 0)$. These two phases are stabilized with a fourth degree expansion of F . Phase III, which, for $-1 < \cos 3\theta < 1$, has a region of stability located between phases I and II, has the $P3c1$ symmetry with the same tripling of the unit cell. This phase requires a sixth-degree term in F for its stabilization. Because of the cubic term in F , the transition to the $P6_3cm$ phases I and II is necessarily of the first order and takes place at a temperature $T_1 > T_C$. The transition to the $P3c1$ phase III cannot occur directly from the parent phase, except at a single point of the phase diagram.

The total polarization $P = P_0 + \Delta P$ is left invariant by all the symmetry operations of the $P6_3mc$ space group, which have the symmetry of the Γ_1 BZ center representation. Therefore, under applied electric field E , the dielectric free energy F_D has the general form:

$$F_D = P \left(\frac{a}{2}\varrho^2 + \frac{b}{3}\varrho^3 \cos 3\theta \right) + \frac{\delta}{2}P^2\varrho^2 + \frac{P^2}{2\chi_{zz}^0} - EP \quad (11)$$

where a , b and δ are coupling coefficients. Taking into account the equilibrium condition $\cos 3\theta = 1$ and minimizing F_D with respect to P yields the equation of state for P below T_1 :

$$P\left(\frac{1}{\chi_{zz}^0} + \delta\varrho^2\right) + \varrho^2\left(\frac{a}{2} + \frac{b}{3}\varrho\right) = E. \quad (12)$$

Minimizing the total free energy $F + F_D$, truncated at the fourth degree, with respect to ϱ provides the other equation of state:

$$\alpha + \varrho(\beta_1 + \beta_2\varrho) + P(a + b\varrho + \delta P) = 0. \quad (13)$$

By extracting ϱ as a function of P from Eq. (13) and replacing this expression into Eq. (12), one gets an equation containing only P and E which can yield the $E(P)$ dependence. Keeping all the terms in the equations requires numerical simulations. An acceptable approximation providing an algebraic form for $E(P)$ can be obtained by neglecting the δ , b and β_2 terms in Eq. (13), and the δ term in Eq. (12). This leads to:

$$E = \frac{P}{\chi_{zz}^0} + \frac{1}{\beta_1^2} \left[-\frac{a^3b}{3\beta_1} P^3 + a^2 \left(\frac{a}{2} - \frac{ab}{\beta_1} \right) P^2 + \alpha a \left(a - \frac{ab}{\beta_1} \right) P + \alpha^2 \left(\frac{a}{2} - \frac{ab}{3\beta_1} \right) \right] \quad (14)$$

from which one can deduce the dielectric susceptibility $\chi = \lim_{E \rightarrow 0} \frac{\partial P}{\partial E}$:

$$\chi = \frac{\chi_{zz}^0}{1 + \frac{\alpha\chi_{zz}^0}{\beta_1^2} \left[-\frac{a^2b}{\beta_1} P^2 + a \left(a - 2\frac{ab}{\beta_1} \right) P + \alpha \left(a - \frac{ab}{\beta_1} \right) \right]} \quad (15)$$

where P takes its zero-field approximated value:

$$P = -\chi_{zz}^0 \left(\frac{a}{2}\varrho^2 + \frac{b}{3}\varrho^3 \right) \quad (16)$$

and ϱ can be approximated (not too close to T_1) as $\varrho \approx (T_1 - T)^{\frac{1}{2}}$.

Eq. (16), which constitutes a first approximation of $P(T)$, shows that depending on the sign and magnitude of the coefficients a and b and assuming a more accurate form for $\varrho(T)$, it may be possible to reproduce the observed behavior reported in Figs. 4 and 5. Along the same line Eq. (14) also shows that a complicated $E(P)$ hysteresis behavior may occur.

E. Magnetic properties

The earlier published reports about the AFM phase transition in 2H-BaMnO₃ provided contradictory information. On the one hand, a magnetic susceptibility $\chi(T)$ monotonically increasing on cooling without any anomaly was observed by Chamberland *et al.*⁵³ and Christensen *et al.*²⁴ This led them to the conclusion that T_N was lower than 3 K. On the other hand, below $T_N = 59 \pm 2$ K, Cussen and Battle²⁵ observed, by means of neutron diffraction, a long-range AFM order. Simultaneously, they found

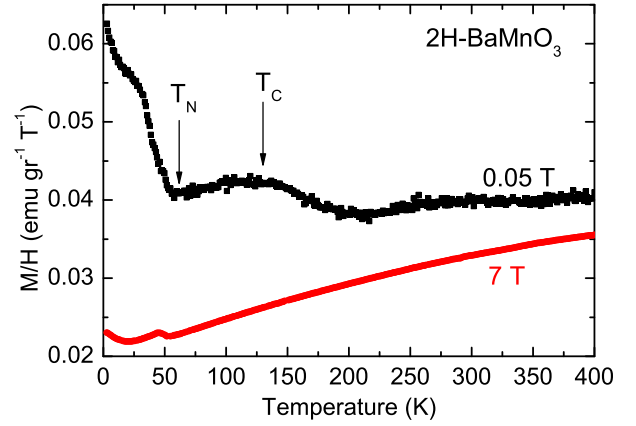


FIG. 9: Temperature dependence of magnetization divided by magnetic field, measured with an external magnetic field of 0.05 and 7 T. Note that neither curve follows the Curie-Weiss law.

that the magnetic susceptibility $\chi(T)$ does not follow the Curie-Weiss law, below ca. 200 K it exhibits different values in field- and zero-field regimes and shows no maximum at T_N . They proposed to explain this behavior by suggesting a short-range one-dimensionally ordered AFM phase at least up to 200 K.

To shed more light on this issue, we performed low-temperature measurements of magnetic properties of our samples. The temperature dependence of χ measured at 0.05 T revealed two minima near 60 and 220 K (see Fig. 9). The first temperature corresponds well to T_N from Ref. 25; the second anomaly will be explained below. In contrast, $\chi(T)$ measured at 7 T shows a continuous decrease on cooling down to T_N . Neither the low- nor the high-field $\chi(T)$ follow the Curie-Weiss law. Interestingly, our measurements of magnetization $M(H)$ up to $\mu_0 H = 7$ T did not reveal any saturation of magnetization even at 2 K (see Fig. 9 in the Supplemental Material [36]).

In order to identify the origin of such an unusual behavior, we performed additional EPR measurements from 16 to 550 K. The EPR spectra measured in the temperature region 140–275 K are shown in Fig. 10. The only resonance line can be attributed to the Mn⁴⁺ ($S = \frac{3}{2}$) ions of BaMnO₃. It has a Lorentzian shape with a peak-to-peak linewidth of 1100 G at 275 K which increases on cooling (see Fig. 10 in the Supplemental Material [36]). Note that a Lorentzian-shaped line with a similar linewidth was observed in the paramagnetic phase of SrMnO₃.⁵⁴ This suggests that the Mn⁴⁺ EPR spectrum of BaMnO₃ is narrowed by the exchange interaction, as expected for paramagnetic materials.⁵⁵ However, upon cooling below 230 K, its intensity sharply decreases and the spectral line almost disappears at $T \approx 150$ K (see inset of Fig. 10). Below this temperature only a weak residual spectrum remains, slightly changing upon further cooling and splitting below 80 K (see Fig. 11 in the Supplemental Material [36]). This feature is obviously linked to paramagnetic impurities at grain boundaries; note that it amounts to

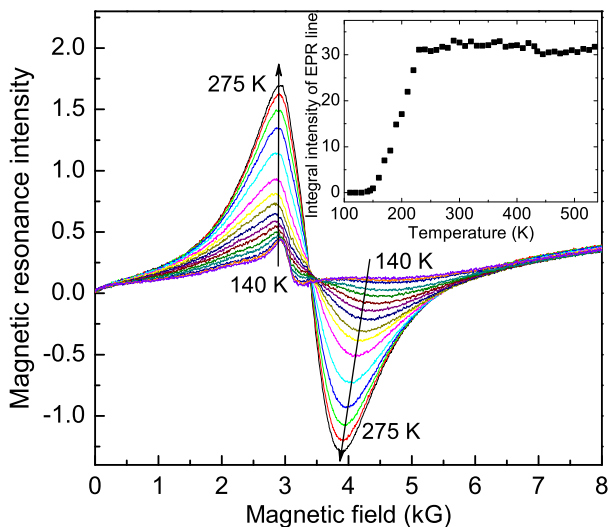


FIG. 10: EPR spectra of 2H-BaMnO₃ measured at 9.4 GHz as a function of temperature. Inset: temperature dependence of the integrated intensity of the EPR line.

about 0.5% of the total Mn⁴⁺ paramagnetic signal only, while the main spectral line must originate from grains.

Further, we calculated the integral intensities via a double integration of the Mn⁴⁺ spectral line (see its temperature dependence in the inset of Fig. 10). As this intensity in the paramagnetic phase should be proportional to the magnetic susceptibility, one can see that the EPR line intensity does not follow the Curie-Weiss law which would impose an increase on cooling towards T_N . Our spectral intensity is almost constant between 550 and 220 K and it drastically decreases below ≈ 220 K. This temperature dependence qualitatively corresponds to $\chi(T)$, where also no Curie-Weiss behavior was observed.

The decrease in the EPR intensity below 220 K indicates a gradual decrease in concentration of paramagnetic (magnetically uncoupled) Mn⁴⁺ ions which develop a mutual AFM correlation at the EPR time scale (10^{-9} – 10^{-10} s). Finally, as the absorption line completely disappears near 140 K, all Mn⁴⁺ spins become AFM-coupled with a zero total spin so that no paramagnetic absorption is possible. This observation supports the hypothesis of Cussen and Battle²⁵ about the existence of a short-range one-dimensionally ordered AFM phase below ≈ 200 K. We can thus conclude that the one-dimensional AFM order starts to form at the temperature of 220 K and that the corresponding Néel temperature of this phase is near 140 K. It remains unclear whether nanoregions with a tripled unit cell, seen above 130 K in the electron diffraction, might be somehow related to a formation of short-range magnetic order below 220 K. A three-dimensionally ordered AFM phase appears at $T_N \approx 59$ K, where the magnetic susceptibility exhibits a minimum (Fig 9).

IV. CONCLUSION

Our complex structural, SHG, dielectric and lattice vibration studies of 2H-BaMnO₃ ceramics revealed features related to the structural phase transition at $T_C = 130$ K. Above T_C , the phase transition is driven by a soft phonon from the BZ boundary with a wavevector $q = (\frac{1}{3}, \frac{1}{3}, 0)$. Below T_C , BZ folding occurs and the soft mode becomes simultaneously IR- and Raman-active. On cooling, its frequency increases according to the Cochran law. The structure of the low-temperature phase was unambiguously determined as $P6_3cm$ with $Z = 6$, but the symmetry of the high-temperature phase, in spite of our efforts, remains unclear. The electron and XRD data can be interpreted as corresponding either to a non-polar ($P6_3/mmc$) or a polar ($P6_3mc$) space group with $Z = 2$. The weak SHG signal detected above T_C does not represent an unambiguous evidence about a polar structure above T_C , as it may be due to the sample surface.

The existence of a FE polarization was proved below T_C , but we were not able to determine it in the high-temperature phase, owing to a leakage current in the pyrocurrent measurements above T_C . Three observed modes simultaneously active in both IR and Raman spectra seem to support the $P6_3mc$ space group (phonons in the $P6_3/mmc$ symmetry should have different activities in IR and Raman spectra), but this evidence is rather weak. First, only three out of seven simultaneously active phonons allowed by factor-group analysis were observed. Second, sixteen modes were detected in the IR spectra, far more than the seven allowed in the $P6_3mc$ structure. The excess modes can be defect-induced or due to nanoclusters of a polar $P6_3cm$ phase present above T_C . The latter possibility was partially supported by electron diffraction revealing the presence of $P6_3cm$ clusters at least 40 K above T_C . These clusters may also explain the observation of the three phonons active simultaneously in IR and Raman spectra.

The Landau theory of an improper FE phase transition in 2H-BaMnO₃ from the $P6_3/mmc$ to the $P6_3cm$ symmetry was published by Varignon and Ghosez.²¹ We presented an alternative Landau theory of a possible non-ferroic phase transition between two polar phases and derived the phase diagram in Fig. 8. In both cases the phase transition is driven by the observed BZ-boundary phonon with $q = (\frac{1}{3}, \frac{1}{3}, 0)$.

The temperature dependence of permittivity exhibits a change in slope at T_C . This unusual behavior corresponds to a theoretical $\epsilon'(T)$ dependence at a second-order non-ferroic phase transition,⁴¹ but our phase transition between $P6_3mc$ and $P6_3cm$ space groups should be of the first order, where some small jump is expected at T_C .⁴¹ Also an improper FE phase transition should exhibit a small jump or even a small peak in $\epsilon'(T)$ at T_C ,⁸ which was not observed in our case. Nevertheless, this characteristic change may be screened by the contribution of FE domain-wall motions, which enhance the microwave and radio-frequency permittivity below T_C . A slowing down

of domain-wall motions was revealed below 60 K, where the frequency-dependent decrease in $\varepsilon'(T)$ was observed. Slim S-shaped FE hysteresis loops were observed below 130 K. Interestingly, the remnant polarization decreases below 60 K and the loops become pinched at 26 K. On subsequent cooling the FE loops open again. We cannot distinguish whether this is an intrinsic or an extrinsic effect; to resolve this issue, further studies would be required. For distinguishing clearly whether the high-temperature phase is polar or not, we propose a SHG experiment using a high-quality single crystal, where a higher laser intensity could be applied. This would significantly enhance the sensitivity of the SHG signal detection.

Our magnetic and EPR studies confirmed earlier ob-

servations of an AFM phase transition at $T_N \approx 59$ K. Additionally, signatures of a one-dimensional or short-range magnetic ordering were observed at least up to 220 K. Again, new magnetic studies on a 2H-BaMnO₃ single crystal should clarify the magnetic properties above T_N .

Acknowledgments

This work was supported by the Czech Science Foundation, Projects Nos. 13-11473S, 14-14122P and 15-08389S, by the Czech Ministry of Education, Youth and Sports, project LH15122, and by the program of Czech Research Infrastructures, project LM2011025.

-
- * Corresponding author: kamba@fzu.cz
- ¹ J. F. Scott, *Rev. Mod. Phys.* **46**, 83 (1974).
 - ² J. Petzelt and S. Kamba, *Ferroelectrics* **503**, 19 (2016).
 - ³ J. Grigas, *Microwave dielectric spectroscopy of ferroelectrics and related materials* (Gordon and Breach Publishers, 1996).
 - ⁴ J. Petzelt, G. Kozlov, and A. Volkov, *Ferroelectrics* **73**, 101 (1987).
 - ⁵ E. Buixaderas, S. Kamba, and J. Petzelt, *Ferroelectrics* **308**, 131 (2004).
 - ⁶ J. Hlinka, T. Ostapchuk, D. Nuzhnyy, J. Petzelt, P. Kužel, C. Kadlec, P. Vaněk, I. Ponomareva, and L. Bellaiche, *Phys. Rev. Lett.* **101**, 167402 (2008).
 - ⁷ F. Kadlec, C. Kadlec, P. Kužel, and J. Petzelt, *Phys. Rev. B* **84**, 205209 (2011).
 - ⁸ A. Levanyuk and D. G. Sannikov, *Soviet. Phys. Uspekhi* **17**, 199 (1974).
 - ⁹ V. Dvořák, *Ferroelectrics* **7**, 1 (1974).
 - ¹⁰ P. Tolédano, *Phys. Rev. B* **79**, 094416 (2009).
 - ¹¹ J. Young, A. Stroppa, S. Picozzi, and J. M. Rondinelli, *J. Phys.: Condens. Matter* **27**, 283202 (2015).
 - ¹² M. Lilienblum, T. Lottermoser, S. Manz, S. M. Selbach, A. Cano, and M. Fiebig, *Nature Phys.* **11**, 1070 (2015).
 - ¹³ A. Munoz, J. Alonso, M. Martinez-Lope, M. Casais, J. Martinez, and M. Fernandez-Diaz, *Phys. Rev. B* **62**, 9498 (2000).
 - ¹⁴ F. Yen, C. Dela Cruz, B. Lorenz, E. Galstyan, Y. Sun, M. Gospodinov, and C. Chu, *J. Mat. Res.* **22**, 2163 (2007).
 - ¹⁵ C. J. Fennie and K. M. Rabe, *Phys. Rev. B* **72**, 100103 (2005).
 - ¹⁶ V. Goian, S. Kamba, C. Kadlec, D. Nuzhnyy, P. Kužel, J. Agostinho Moreira, A. Almeida, and P. Tavares, *Phase Transit.* **83**, 931 (2010).
 - ¹⁷ H. Bouyanfif, A. M. Salah, M. Zaghrioui, and M. El Marssi, *Phys. Rev. B* **91**, 224104 (2015).
 - ¹⁸ J. Petzelt, F. Smutný, V. Katkanant, F. Ullman, J. R. Hardy, A. Volkov, G. Kozlov, and S. Lebedev, *Phys. Rev. B* **30**, 5172 (1984).
 - ¹⁹ D. Lockwood, *Solid State Commun.* **18**, 115 (1976).
 - ²⁰ J. Petzelt and I. Mayerova, *Czech. J. Phys.* **23**, 1277 (1973).
 - ²¹ J. Varignon and P. Ghosez, *Phys. Rev. B* **87**, 140403 (2013).
 - ²² T. Negas and R. Roth, *J. Sol. State Chem.* **3**, 323 (1971).
 - ²³ J. J. Adkin and M. A. Hayward, *Chem. Mat.* **19**, 755 (2007).
 - ²⁴ A. N. Christensen and G. Ollivier, *J. Sol. State Chem.* **4**, 131 (1972).
 - ²⁵ E. Cussen and P. Battle, *Chem. Mater.* **12**, 831 (2000).
 - ²⁶ C. Roy and R. Budhani, *Phys. Rev. B* **58**, 8174 (1998).
 - ²⁷ T. N. Stanislavchuk, A. P. Litvinchuk, R. Hu, Y. H. Jeon, S. D. Ji, S.-W. Cheong, and A. A. Sirenko, *Phys. Rev. B* **92**, 134308 (2015).
 - ²⁸ D. Kriegner, Z. Matěj, R. Kužel, and V. Holý, *J. Appl. Cryst.* **48**, 613 (2015).
 - ²⁹ H. Rietveld, *J. Appl. Cryst.* **2**, 65 (1969).
 - ³⁰ R. W. Cheary, A. A. Coelho, and J. P. Cline, *J. Res. Natl. Inst. Stand. Technol.* **109**, 1 (2004).
 - ³¹ E. Mugnaioli, T. Gorelik, and U. Kolb, *Ultramicroscopy* **109**, 758 (2009).
 - ³² L. Palatinus, *PETS – program for analysis of electron diffraction data*, Institute of Physics of the AS CR: Prague, Czech Republic (2011).
 - ³³ V. Petříček, M. Dušek, and L. Palatinus, *Zeitschrift für Krist.—Cryst. Mater.* **229**, 345 (2014).
 - ³⁴ L. Palatinus, V. Petříček, and C. A. Corrêa, *Acta Cryst. Sect. A: Foundations and Advances* **71**, 235 (2015).
 - ³⁵ L. Palatinus, C. A. Corrêa, G. Steciuk, D. Jacob, P. Rousel, P. Boullay, M. Klementová, M. Gemmi, J. Kopeček, M. C. Domeneghetti, et al., *Acta Cryst. Section B: Struct. Science, Cryst. Eng. and Mater.* **71** (2015).
 - ³⁶ See the supplemental material at <https://link.aps.org/supplemental/...>
 - ³⁷ V. Bovtun, S. Veljko, A. Axelsson, S. Kamba, N. Alford, and J. Petzelt, *Integr. Ferroelectrics* **98**, 53 (2008).
 - ³⁸ V. Bovtun, V. Pashkov, M. Kempa, S. Kamba, A. Eremenko, V. Molchanov, Y. Poplavko, Y. Yakymenko, J. Lee, and D. Schlom, *J. Appl. Phys.* **109**, 024106 (2011).
 - ³⁹ A. S. Gibbs, K. S. Knight, and P. Lightfoot, *Phys. Rev. B* **83**, 094111 (2011).
 - ⁴⁰ S. M. Selbach, A. N. Løvik, K. Bergum, J. R. Tolchard, M.-A. Einarsrud, and T. Grande, *J. Sol. State Chem.* **196**, 528 (2012).
 - ⁴¹ P. Tolédano and J.-C. Tolédano, *Phys. Rev. B* **25**, 1946 (1982).
 - ⁴² Y. N. Huang, X. Li, Y. Ding, Y. N. Wang, H. M. Shen,

- Z. F. Zhang, C. S. Fang, S. H. Zhuo, and P. C. W. Fung, *Phys. Rev. B* **55**, 16159 (1997).
- ⁴³ P. Lunkenheimer, V. Bobnar, A. Pronin, A. Ritus, A. Volkov, and A. Loidl, *Phys. Rev. B* **66**, 052105 (2002).
- ⁴⁴ K. Carl and K. Hardtl, *Ferroelectrics* **17**, 473 (1978).
- ⁴⁵ L. Jin, F. Li, and S. Zhang, *J. Amer. Ceram. Soc.* **97**, 1 (2014).
- ⁴⁶ D. Rousseau, R. P. Bauman, and S. Porto, *J. Raman Spectroscopy* **10**, 253 (1981).
- ⁴⁷ V. Porokhonsky, L. Jin, and D. Damjanovic, *Appl. Phys. Lett.* **94**, 212906 (2009).
- ⁴⁸ Y.-K. Choi, T. Hoshina, H. Takeda, T. Teranishi, and T. Tsurumi, *Appl. Phys. Lett.* **97**, 212907 (2010).
- ⁴⁹ D. Nalecz, R. Radwanski, and Z. Ropka, *Mat. Chem. Phys.* **180**, 144 (2016).
- ⁵⁰ I. Kratochvílová-Hrubá, I. Gregora, J. Pokorný, S. Kamba, Z. Zikmund, J. Petzelt, M. Čerňanský, V. Studnička, V. Sigaev, and E. Smelyanskaya, *J. Non-cryst. Sol.* **290**, 224 (2001).
- ⁵¹ J. Hlinka, J. Petzelt, S. Kamba, D. Noujni, and T. Ostapchuk, *Phase Transit.* **79**, 41 (2006).
- ⁵² E. Buixaderas, V. Bovtun, M. Kempa, D. Nuzhnyy, M. Savinov, P. Vaněk, I. Gregora, and B. Malič, *Phys. Rev. B* **94**, 054315 (2016).
- ⁵³ B. Chamberland, A. Sleight, and J. Weiher, *J. Sol. State Chem.* **1**, 506 (1970).
- ⁵⁴ G. Alvarez, J. Heiras, M. Castellanos, and R. Valenzuela, *J. Magnetism and Magnetic Mat.* **320**, e117 (2008).
- ⁵⁵ P.-W. Anderson and P. Weiss, *Rev. Mod. Phys.* **25**, 269 (1953).